Energy spread blowup by intrabeam scattering and microbunching at the SwissFEL injector

Eduard Prat,[1,*] Paolo Craievich,[1] Philipp Dijkstal,[1,2] Simone Di Mitri,[3,4] Eugenio Ferrari,[1,†] Thomas G. Lucas,[1] Alexander Malyzhenkov,[1,‡] Giovanni Perosa,[3,4] Sven Reiche,[1] and Thomas Schietinger[1]

[1]*Paul Scherrer Institut, CH-5232 Villigen PSI, Switzerland*
[2]*Department of Physics, ETH Zürich, 8092 Zürich, Switzerland*
[3]*Department of Physics, University of Trieste, 34100 Trieste, Italy*
[4]*Elettra-Sincrotrone Trieste S.C.p.A., 34149 Basovizza, Italy*

(Received 1 July 2022; accepted 15 September 2022; published 4 October 2022)

We present high-resolution measurements of the electron beam energy spread at the SwissFEL injector as a function of the electron bunch charge, the optics, and the longitudinal dispersion of the lattice. The measured values are in general an order of magnitude higher than what is predicted by standard simulation codes. The measured dependences indicate that the energy spread blowup is caused primarily by intrabeam scattering and microbunching instabilities, effects not covered in the conventional modeling of radio-frequency injectors. We present further a numerical model that qualitatively reproduces the experimental data and an approach to mitigate the energy spread deterioration. The work underlines the importance of considering the energy spread in the optimization and design of high-brightness electron beam sources and the need to develop new models to adequately understand and simulate the observed physics effects.

DOI: 10.1103/PhysRevAccelBeams.25.104401

I. INTRODUCTION

High-brightness electron beam sources are fundamental for scientific applications such as electron diffraction [1,2], gamma-ray, or x-ray sources based on inverse Compton scattering [3,4], and x-ray free-electron lasers (FELs) [5–7]. Radio-frequency (rf) photoinjectors [8] (for a more recent review, see [9]), where electrons are generated via the photoelectric effect by a laser impinging on a photocathode placed in an rf gun, are the state-of-the-art technology to produce intense bright electron beams. There is extensive worldwide research to improve the brightness of rf photoinjectors [10–12] and to develop alternative ultrabright solutions such as plasma sources [13–15].

The electron beam brightness B can be expressed as [16]:

$$B = \frac{2I}{\varepsilon_{n,x}\varepsilon_{n,y}\sigma_\gamma}, \tag{1}$$

where I is the electron beam peak current, ε_{n_x} and ε_{n_y} are, respectively, the horizontal and vertical normalized emittances, and $\sigma_\gamma = \sigma_E/(m_e c^2)$ is the uncorrelated energy spread of the electron beam expressed in terms of the Lorentz factor γ, with $m_e c^2$ being the rest energy of an electron (0.511 MeV). From the above expression, we see that a high-brightness electron beam corresponds to small normalized transverse emittances, high peak current, and low energy spread.

In this article, we focus on the impact of the electron beam energy spread in x-ray FEL facilities. The energy spread is a crucial parameter for at least four reasons. First, for an efficient FEL process, the uncorrelated relative energy spread of the electrons σ_γ/γ at the undulator has to be smaller than the Pierce parameter ρ [17], which for x rays has typical values between 10^{-4} and 10^{-3}. Second, once this limit has been fulfilled, the lower the energy spread, the better the FEL performance will be. Third, the initial energy spread limits how much an electron bunch can be compressed. In general, the beam can only be compressed to within the regime where the condition $\sigma_\gamma/\gamma < \rho$ is fulfilled. When the beam is compressed, the energy spread increases at least proportionally to the compression factor C but ρ only increases with $C^{1/3}$. Moreover, the energy spread limits how short the electron beam can be for full compression [18]. And finally, the energy spread is fundamental in externally seeded FELs

*eduard.prat@psi.ch
†Present address: Deutsches Elektronen-Synchrotron, D-22607 Hamburg, Germany.
‡Present address: CERN, CH-1211 Geneva 23, Switzerland.

employed to produce fully coherent FEL radiation for wavelengths much shorter than the seed wavelength [19–21]. The energy spread sets a lower limit to the required seed power to induce a certain energy modulation (the larger the energy spread the higher the required power). On the other hand, the seed-induced energy modulation increases the final energy spread, thereby limiting in turn the shortest achievable wavelength.

In a typical x-ray FEL facility, rf photoinjectors generate electron beams with energies of 5–10 MeV, peak currents of 10–20 A, and design energy spread values at the keV level or below. The beam is then accelerated and compressed in the linac to reach the GeV energies and kA peak currents necessary for lasing in the undulator. The energy spread is increased in the linac to the MeV level as a result of compression. Liouville's theorem calls for the conservation of longitudinal emittance in terms of uncorrelated energy spread and bunch length. Therefore, the energy spread increases in proportion to the increase in peak current. Moreover, certain detrimental effects such as intrabeam scattering (IBS) [22–31] or microbunching instability (MBI) [28–42] may cause an additional increase of the energy spread.

The uncorrelated energy spread of the electron beam is normally obtained by measuring the slice (time-resolved) transverse beam size of the electrons at a dispersive location [28,38,40,41,43–46]. To access the slice energy spread, rf transverse deflectors (TD) are typically used to streak the electron in the plane orthogonal to the transverse dispersion. The standard approach consists in obtaining the relative energy spread as $\sigma_{E,m}/E = \sigma_m/D$, where $\sigma_{E,m}$ is the *measured* energy spread, E is the mean energy of the electrons, σ_m is the measured rms transverse beam size, and D is the dispersion. Three methods have recently been proposed to improve the measurement resolution below 1 keV: by performing the beam size measurement for different electron beam energies [44], dispersion values [45], or transport matrices between the reconstruction and measurement locations [46]. A high-resolution measurement also needs to take into account the energy spread induced by the rf deflector [47], which can be achieved by reconstructing the energy spread for different rf voltages [40,44–46].

Contrary to expectation, high-resolution measurements of the uncorrelated energy spread at different injectors have shown energy spread values much larger than predicted by particle tracking. At SwissFEL, we reconstructed a 15-keV energy spread (without compression at the photoinjector end) for the standard operation mode employing 200 pC bunch charges and 6 keV for 10 pC beams [44]. This contrasts sharply with the results obtained with the ASTRA code [48], which predicts values below 1 keV. For comparison, slice energy spread values of 6 keV were measured at the European XFEL for bunch charges of 250 pC [45]. More recently, similar measurements at the Photoinjector Test Facility at DESY Zeuthen (PITZ), featuring an injector equivalent to the European XFEL, gave energy spread values of 2 keV for 250 pC bunch charges [46]. Both these values are clearly lower than those observed at SwissFEL but still significantly higher than what was predicted from numerical simulations. The distance between the rf gun and the measurement location is more than 110 m at SwissFEL, to be compared to approximately 40 m for the European-XFEL [45] and about 20 m at PITZ [49]. The increase in the uncorrelated energy spread as a function of injector length could indicate the existence of collective deteriorating effects that grow with distance, such as IBS and MBI.

ASTRA simulations include space-charge effects but do not consider IBS, high-frequency components of the MBI, or cathode contributions to the energy spread. Modeling these effects is difficult without resorting to excessively large numbers of particles and grid points. We have measured the energy spread as a function of different parameters at the SwissFEL injector aiming to understand the reasons for the energy spread increase. In particular, we wanted to know if the energy spread deterioration comes from IBS and/or MBI. We present here the results of this study: measurements of the energy spread as a function of the bunch peak current, the beam optics, and the longitudinal dispersion of the lattice indicate that both IBS and MBI contribute to the blowup of the energy spread of the electron beam (see below for details).

There have been many pieces of numerical and experimental evidence showing the impact of MBI on the energy spread for beams after compression with peak currents at the kA level, see for instance [28,38–40]. In a recent work, Di Mitri and colleagues found that, in addition to MBI, IBS can also be a relevant contribution to the energy spread for beams after compression [28]. Here we show for the first time that MBI and IBS can also play a significant role in the energy spread of electron beams at an FEL injector for uncompressed bunches. Our work emphasizes the importance of considering the energy spread when optimizing and designing high-brightness electron sources and the need to update the existing tools to appropriately consider IBS and MBI.

The article is organized as follows: In the next section, we will briefly discuss the current state of theory and modeling of IBS and MBI. Later we present the measurement setup and procedure, followed by the experimental results. After that we present simulation results from a simplified model of IBS and MBI that fit the experimental data.

II. CURRENT STATE OF THEORY AND MODELING OF IBS AND MBI

IBS is the multiple small-angle Coulomb scattering of charged particles in accelerators, leading to a potential growth of the beam energy spread. There are quite a

number of publications presenting the IBS theory and analytical expressions to estimate the energy spread increase due to IBS, see for instance [22–31]. Assuming effectively constant beam properties along the lattice, the energy spread induced by IBS ($\sigma_{\gamma,\mathrm{IBS}}$) can be expressed as [25]:

$$\sigma_{\gamma,\mathrm{IBS}} = \left(\frac{2r_e^2 N_e}{\varepsilon_n \sigma \sigma_s} z\right)^{\frac{1}{2}} \propto \left(\frac{I}{\varepsilon_n \sigma} z\right)^{\frac{1}{2}}, \tag{2}$$

where r_e is the classical electron radius, N_e is the number of electrons in the bunch, ε_n is the transverse emittance averaged over the horizontal and vertical planes ($\varepsilon_n = \sqrt{\varepsilon_{n,x}\varepsilon_{n,y}}$), σ is the average transverse beam size ($\sigma = \sqrt{\sigma_x \sigma_y}$), σ_s is the bunch length, and z is the longitudinal distance along the accelerator. The transverse beam size can be expressed as $\sigma = \sqrt{\beta \varepsilon_n / \gamma}$, where β is the mean β function of the lattice. Thus we may write

$$\sigma_{\gamma,\mathrm{IBS}} \propto \frac{I^{\frac{1}{2}} \gamma^{\frac{1}{4}}}{\varepsilon_n^{\frac{3}{4}} \beta^{\frac{1}{4}}} z^{\frac{1}{2}}. \tag{3}$$

We note that the model described by the above Eqs. (2) and (3), based on the dynamics in a storage ring, may not be fully applicable in linear accelerators.

A full treatment of IBS is extremely challenging since it requires running one-to-one simulations. Running simulations with fewer electrons than are present in the actual bunch would lead to unphysically strong scattering events if not properly filtered numerically (scaling by the square of the macroparticle charge), resulting in excessively large scattering amplitudes. This type of simulation requires computational times that are impossible in practice for standard bunch charges (e.g., 200 pC or 1.25×10^9 electrons). A possible approximation, as done in [12] for the GPT code [50], consists in scaling down all beam dimensions such that the beam density stays constant and assuming that the resulting IBS effects are valid for the original beam. In [12], a full one-to-one simulation was performed for a scaled-down 100-fC beam representing a target of 100 pC. This approach entails some uncertainty since IBS does not depend exactly on the electron beam density as shown in previous Eq. (3). The authors of Ref. [12] acknowledge that this approximation can lead to errors at the 50% level.

MBI consists of the amplification of initial small-scale nonuniformities of the charge distribution due to longitudinal space charge and coherent synchrotron radiation effects. MBI affects the longitudinal phase space of the electrons. For high frequencies that cannot be resolved with temporal diagnostics, this appears as an increase in the uncorrelated energy spread. A similar effect appears at lower frequencies for existing longitudinal dispersion (R_{56}) in the beamline resulting in an overbunching. If the resulting energy bands cannot be resolved, they also appear as an increase in the uncorrelated energy spread.

Similar to IBS, there are numerous publications on MBI theory and associated analytical expressions, see for instance [28–35,37,42]. In the 1D approximation, the energy spread induced by MBI ($\sigma_{\gamma,\mathrm{MBI}}$) accumulates with the distance z for given bunching $b(k)$ at a given spatial frequency k; i.e.,

$$\sigma_{\gamma,\mathrm{MBI}} \propto I b(k) z. \tag{4}$$

MBI is significantly driven by R_{56} at dispersive locations such as the bunch compressors of x-ray FEL facilities. The R_{56} affects $b(k)$ depending on the energy modulations in the bunch. For high frequencies relevant for our case, the driving space-charge forces have some dependence on the transverse beam size but typically much less than in the IBS case.

A complete treatment of MBI requires integrating the instability over different frequencies and carry over the bunching $b(k)$ and energy modulation $\delta\gamma(k)$ through the whole lattice. The equations relating the bunching and energy modulation from jth to $(j+1)$th step separated by Δz_j are

$$b_{j+1}(k) = \left[b_j(k) - i\frac{kR_{56,j}}{\gamma_j}\delta\gamma_j(k)\right] e^{-\frac{1}{2}(kR_{56,j}\frac{\sigma_{\gamma,j}}{\gamma_j})^2} \tag{5}$$

$$\delta\gamma_{j+1}(k) = \delta\gamma_j(k) - \frac{I}{e\pi I_A}\frac{Z_j(k)}{Z_0}\Delta z_j b_j(k). \tag{6}$$

$Z_j(k)$ is the impedance of the longitudinal space charge

$$Z_j(k) = i\frac{Z_0}{\pi k \sigma_j^2}\left[1 - 2I_1\left(\frac{k\sigma_j}{\gamma_j}\right)K_1\left(\frac{k\sigma_j}{\gamma_j}\right)\right], \tag{7}$$

where Z_0 is the impedance of free space, and I_1, K_1 are modified Bessel functions of the first order.

The energy spread due to MBI can finally be computed as

$$\sigma_{\gamma,\mathrm{MBI}} = \sqrt{\frac{1}{2}\sum_k \delta\gamma^2(k)}. \tag{8}$$

Since we are interested in the impact on the measured uncorrelated energy spread of the beam, only wavelengths shorter than the longitudinal resolution of the TD are relevant.

Unlike in the IBS case, one-to-one simulations of MBI are possible within a reasonable computational time. As an example, MBI has been simulated using IMPACT-T [51] for a realistic beam for the LCLS case in 10 h [52]. These simulations reproduced the experimental data presented in [40] quite well.

In recent work, Litvinenko and coauthors proposed that MBI can also occur along a straight trajectory, i.e., when there is no longitudinal dispersion [53]. There can be a resonant coupling between energy and transverse position in a periodic focusing channel when the plasma and betatronic wave numbers are comparable. This is, however, negligible in most rf photoinjectors, as in our case, where the ratio between plasma and betatronic wave numbers is about 1–50.

MBI in x-ray FELs is normally counteracted by increasing the electron beam energy spread at the injector with a so-called laser heater [35,36,38,39,41]. As shown in Eq. (5), an increase in the energy spread reduces the bunching and thus the energy spread variation due to MBI.

IBS and MBI are mostly uncorrelated effects, although the energy spread increase due to IBS enhances the Landau damping for the MBI [28], which is relevant only for very high frequencies. Assuming uncorrelated contributions, we can write

$$\sigma_\gamma^2 = \sigma_{\gamma,0}^2 + \sigma_{\gamma,\mathrm{IBS}}^2 + \sigma_{\gamma,\mathrm{MBI}}^2, \tag{9}$$

where $\sigma_{\gamma,0}$ denotes the energy spread of the beam not related to either IBS or MBI.

From the above, we can see that IBS and MBI have different dependences on different beam and lattice parameters. First, on the electron bunch peak current I, $\sigma_{\gamma,\mathrm{IBS}} \propto I^{0.5}$, while $\sigma_{\gamma,\mathrm{MBI}} \propto I^{1}$. Second, concerning the transverse beam size or β function, IBS has a clear dependence on $\beta^{-1/4}$. For MBI, the transverse beam size influences the frequency giving the maximum impedance value according to Eq. (7). However, if the accumulated effect is considered over a wide frequency range, as done here, a shift of the maximum position has only little impact. Thus, the MBI effect on the uncorrelated energy spread has a rather weak dependence on the transverse beam size. Third, $\sigma_{\gamma,\mathrm{IBS}}$ does not depend on the lattice R_{56}, while $\sigma_{\gamma,\mathrm{MBI}}$ strongly depends on it. Thus, measuring the energy spread as a function of these three parameters will help us understand and ideally decouple the possible contributions of IBS and MBI to the electron beam energy spread. In the following, we assume that the energy spread unrelated to IBS or MBI ($\sigma_{\gamma,0}$) is not affected by the β function and the R_{56} of the lattice. Therefore, we assume that observing a dependence on β or R_{56} implies the presence of IBS or MBI, respectively.

III. MEASUREMENT SETUP AND PROCEDURE

The results presented in the following were obtained from uncorrelated energy spread measurements for uncompressed beams at the SwissFEL injector. SwissFEL is the x-ray FEL facility at the Paul Scherrer Institute in Villigen [54].

A sketch of the SwissFEL injector is shown in Fig. 1. The electron beam is generated in a photocathode rf gun.

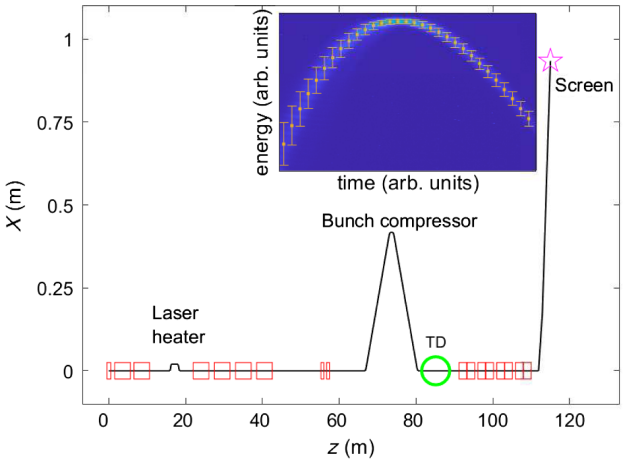

FIG. 1. Sketch of the SwissFEL injector and example of an image of a streaked beam. In the sketch, z corresponds to the longitudinal direction along the accelerator, X is the horizontal position, the red boxes indicate rf accelerating structures, the green circle corresponds to the TD, and the magenta star indicates the position of the profile monitor. In the image, the white points and error bars indicate the slice centroids and slice beam sizes, respectively.

A calcium fluoride ($Yb:CaF_2$) laser produces electrons via the photoelectric effect in a cesium telluride cathode deposited on a copper plug. An S band (3 GHz) rf gun accelerates the electron beam to a central energy of 7.1 MeV. In the standard operation mode, the bunch charge is 200 pC and the peak current is around 20 A. After the gun, the electron beam is accelerated with two S band rf structures up to an energy of 150 MeV. Afterward, there is a laser heater, a device consisting of a magnetic chicane, an IR laser, and an undulator. The nominal R_{56} of the laser heater chicane is $R_{56,\mathrm{LH}} = 2.2$ mm. For the measurements presented here, the laser heater was not used (the laser was turned off). Following the laser heater, four additional S band rf structures further accelerate the beam up to an energy of 320 MeV. An X band (12 GHz) rf station is used to linearize the compression [55]. It decelerates the beam to an energy of 300 MeV. Further downstream there is the first bunch compressor, a magnetic chicane consisting of four dipole magnets, with a nominal longitudinal dispersion $R_{56,\mathrm{BC}} = 63.6$ mm. In standard operation, the compression is achieved by accelerating the beam off-crest in the third and fourth S band stations to induce an energy chirp along the bunch. For the studies shown here, the S band stations operate at on-crest acceleration, such that the bunch compressor induces no compression at the beam core. Downstream of the bunch compressor there is an S band rf TD used to characterize the time-resolved properties of the electron beam. The longitudinal phase space of the electrons is measured with a Ce:YAG scintillator screen [56] placed at the injector spectrometer following the TD. A quadrupole magnet at the injector spectrometer allows

the dispersion D at the profile monitor to be adjusted. Between the TD and the beam dump, there are eight C band (5.7 GHz) rf structures that allow us to vary the electron beam energy between practically zero and about 800 MeV. The design optics along the injector has an average β function of around 15 m.

Figure 1 shows an example of a single-shot image of the streaked beam at the spectrometer and the corresponding slice beam centroids and sizes for a bunch charge of 200 pC. We divide the extent of the beam in the streaked direction into 31 slices and apply Gaussian fits to obtain the beam size and the centroid for every slice. The rf curvature of the different accelerating sections results in a variation of the energy chirp along the slices, which leads to an increase in the observed slice beam sizes at the screen. We, therefore, determine the beam size only for the core part of the beam, for which the rf curvature effect is minimal. The energy spread is then derived from the minimum slice beam size at the core beam region. We declare a measurement invalid if the minimum beam size is not at the core location.

As mentioned in the Introduction, in the standard measurement approach, the uncorrelated energy spread is obtained from the slice transverse beam size as $\sigma_{E,m} = E\sigma_m/D$ for a fixed electron beam energy E and dispersion D. This approximation ignores effects related to the natural beam size (or betatronic contribution) and profile monitor resolution. In fact, the measured beam size is

$$\sigma_m^2 = \sigma_R^2 + \frac{m_e c^2 \beta \varepsilon_n}{E} + \frac{D^2 \sigma_{E,m}^2}{E^2}, \tag{10}$$

where σ_R is the profile monitor resolution. Thus, the measurement resolution of the standard approach is

$$R_{\sigma_{E,m}} = \frac{E}{D}\sqrt{\sigma_R^2 + \frac{m_e c^2 \beta \varepsilon_n}{E}}. \tag{11}$$

Besides resolution issues, the measured energy spread $\sigma_{E,m}$ includes the contribution from the TD, $\sigma_{E,T}$, which adds quadratically to the true energy spread of the beam σ_E:

$$\sigma_{E,m}^2 = \sigma_E^2 + \sigma_{E,T}^2. \tag{12}$$

The TD contribution can be computed as [47]

$$\sigma_{E,T} = e k_T V \cos(\phi) \sigma_T, \tag{13}$$

where k_T is the wave number of the deflector, V is the deflector voltage, ϕ is the TD operating phase (normally the TD runs at the zero crossing so $\cos(\phi) = 1$), and σ_T is the average transverse beam size (in the deflecting direction) at the TD. The transverse beam size at the TD can be expressed as

$$\sigma_T = \sqrt{\frac{m_e c^2 \beta_T \varepsilon_{n,T}}{E_T}}, \tag{14}$$

where β_T is the β function at the structure, $\varepsilon_{n,T}$ is the normalized emittance in the streaking plane, and E_T is the energy at the deflector. For slice energy spread measurements, the deflector voltage should be chosen to have an optimum balance between small induced energy spread and enough streaking to overcome the rf curvature effects. Increasing the deflecting voltage for a higher temporal resolution induces more energy spread up to the point where the measured values are dominated by the TD contribution rather than the true energy spread of the beam.

As described in [44], the measurement resolution [Eq. (11)] can be overcome by measuring the slice beam size at different electron beam energies. Moreover, the TD contribution and the true energy spread can be known by measuring the slice energy spread at different TD voltages.

IV. EXPERIMENTAL RESULTS

Our measurements were done in two different shifts. On the first day, we measured the energy spread as a function of the bunch peak current and as a function of the lattice optics (β function) for nominal (nonzero) $R_{56,\mathrm{LH}}$ and $R_{56,\mathrm{BC}}$. The peak current scan was done for the lowest β function optics, while the scan of the lattice optics was performed for the standard 200 pC bunch with a peak current of 20 A. In the second measurement shift, we performed the same scans on beam current and optics but for $R_{56,\mathrm{LH}} = R_{56,\mathrm{BC}} = 0$ mm. With these scans, we aimed to study the impact of IBS under a reduced contribution from MBI. On this second day, we also measured the energy spread as a function of $R_{56,\mathrm{LH}}$ and $R_{56,\mathrm{BC}}$ for standard optics and peak current. We performed $R_{56,\mathrm{LH}}$ scans on two other occasions and obtained results equivalent to the ones reported here.

For each configuration, we matched the optics at the laser heater location. Before the laser heater, there are approximately 20 m of propagation for which the optics slightly vary for each electron beam current. Nevertheless, we expect this effect to be negligible since the optics variation is rather small and the energy spread growth in this region ($\approx$20 m) is also small compared to the total growth in the injector ($>$110 m). The different lattice optics were set according to precalculated values. The electron beam current was tuned by reducing the laser intensity and thus the extracted bunch charge at the cathode. The laser iris was set to 2 mm for all cases except for the lowest peak current case in the first measurement shift (1 A), for which it was set to 0.7 mm. The normalized projected emittance in both planes measured at the laser heater was between 200 and 300 nm for all cases except for the 1-A configuration. In this case, because of the reduced laser beam size, the emittance improved to 70 nm.

We expect the slice emittance to be smaller than the projected emittance—around 150 nm for the 2-mm iris size [57]. We measured the electron beam current profile and thus the peak current for each configuration. In all measurements, the electron beam current profile was approximately Gaussian with the peak current value at the core of the bunch.

The measurement optics was similar but slightly different for the two shifts. On the first day, the β function at the TD (β_T) was 60 m, while at the screen location, we had a β function of 0.4 m and a dispersion (D) of 1.4 m. For the second shift, $\beta_T = 50$ m, at the screen $\beta = 0.7$ m, and $D = 1.5$ m. For each measurement condition, we empirically minimized the observed slice horizontal beam size by slightly adjusting the magnetic strength of a relevant focusing quadrupole upstream of the magnetic spectrometer, thus minimizing the natural beam size contribution to the measured beam size without changing the dispersion contribution [see Eq. (10)].

For the condition giving the lowest energy spread values (during the second shift for the lowest peak current of just 0.3 A), we performed a full high-resolution measurement following the procedure described in [44] to determine the true energy spread, the measurement resolution, and the TD contribution. For the rest of the measurements, we measured the energy spread using the standard approach for a beam energy of around 100 MeV and we corrected the values by applying the resolution and the TD contribution found with the high-resolution approach.

At each experimental condition, the slice beam sizes were measured between five and ten shots. We repeated the measurements for certain parameter sets and observed good consistency between different measurements performed under the same conditions. The results shown in the following represent the average and standard deviation over the different shots. In the case where a measurement was repeated for a certain condition, the given numbers correspond to the average and uncertainties over the different repetitions.

A. High-resolution measurement

The high-resolution measurement was done for a peak current of 0.3 A, $R_{56,\mathrm{LH}} = R_{56,\mathrm{BC}} = 0$ mm, and standard lattice optics. We measured the electron beam size at the screen for different electron beam energies and TD voltages. For each TD voltage, we fit the energy scan according to Eq. (10) to obtain the energy spread at the screen, the screen resolution, and the betatronic contribution. Once we have the energy spread as a function of the TD voltage, we fit the results using Eq. (12) to reconstruct the true electron beam energy spread and the TD contribution.

The measurements were done for five to six different energies between 70.5 and 604 MeV and voltages between 0.2 and 0.4 MV (in steps of 0.05 MV). For the two highest beam energies, we only measured the beam sizes for two TD voltages. For these two energies, we assume that the beam size for the unmeasured TD voltages was the same as for the closest measured voltage. This assumption is valid considering that the beam size is dominated by screen resolution at high energies and practically not affected by the TD. In fact, the measured beam size was the same for the two measured voltages.

Figure 2 shows the energy scan for one of the TD voltages ($V = 0.25$ MV) and the TD voltage scan. The profile monitor resolution obtained averaging the results from all energy scans was 37.5 ± 0.5 μm. All energy scans showed a negligible betatronic contribution with respect to the other two components. From the design optics, we would expect a slightly larger beam size contribution. The reason for the smaller effect could be that the empirically optimized optics gave a smaller β function than the design one.

The fit to the TD scan gives an electron beam energy spread of 1.35 ± 0.35 keV and a reconstructed TD contribution $\sigma_{E,T}/(eV) = k_T\sigma_T$ of $(6.97 \pm 0.59) \times 10^{-3}$. The reconstructed energy spread using the standard approach for the lowest beam energy (70.5 MeV) at the lowest TD gradient (0.2 MV) would give an energy spread of 2.77 ± 0.02 keV, thus overestimating the true energy

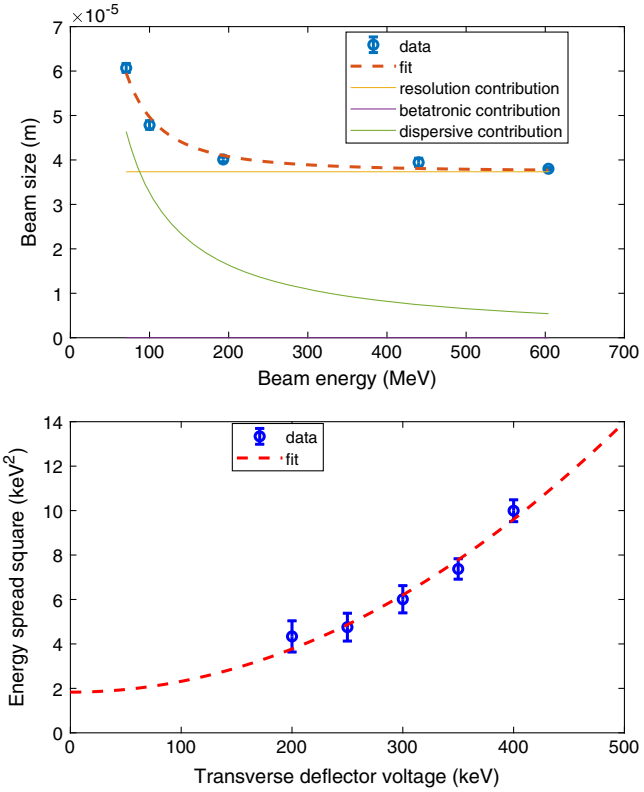

FIG. 2. High-resolution energy spread measurement. Top: energy scan for $V = 0.25$ MV to determine the energy spread and the measurement resolution at this voltage. Bottom: measured energy spread as a function of the TD voltage to reconstruct the true energy spread. See text for more details.

spread (1.35 keV) by about a factor of 2. The energy spread including the TD contribution is 2.1 ± 0.2 keV for a voltage of 0.2 MV. The reconstructed TD contribution is consistent with expectations: from Eqs. (13) and (14), we obtain the same contribution of around 7×10^{-3} with $k = 62.8$ m^{-1} for our TD (3 GHz), the design β function at the deflector ($\beta_T = 50$ m) and a normalized slice emittance of 150 nm.

For the rest of the measurements, we first subtracted the profile monitor resolution of 37.5 μm from the slice beam size measurement. Here we assume, as we found out in earlier studies [44,57], that the profile monitor resolution does not depend on the electron bunch charge. We then obtained the slice energy spread from the corrected beam size. Finally, we removed the TD contribution to obtain the true energy spread. We note that, for day 1, we corrected the TD contribution taking into account the slightly different β function at the screen (60 m instead of 50 m).

B. Parameter dependence measurements

For all of the following measurements, the TD voltage was between 0.2 and 0.35 MV. For each case, we display both the energy spread obtained from the standard approach and the one calculated after subtracting the resolution and TD contributions. The numbers quoted in the text refer to corrected data (with resolution and TD contributions subtracted).

Figure 3 shows the measured energy spread as a function of $R_{56,\mathrm{LH}}$ for two different $R_{56,\mathrm{BC}}$: the nominal value of 63.6 and 0 mm (straight chicane). The measurements were done for an average β function of around 15 m and for the standard peak current of around 20 A (corresponding to a bunch charge of 200 pC). The figure makes it clear that the energy spread depends on both $R_{56,\mathrm{LH}}$ and $R_{56,\mathrm{BC}}$. The maximum value of the energy spread is about 11.7 ± 0.3 keV for nominal $R_{56,\mathrm{LH}}$ and $R_{56,\mathrm{BC}}$ and 6.4 ± 0.1 keV when both chicanes are set to zero strength. Interestingly, an $R_{56,\mathrm{LH}}$ of 0.5 mm gives a lower energy spread than $R_{56,\mathrm{LH}} = 0$ mm (more evident for nominal $R_{56,\mathrm{BC}}$). The reason is that with a small but nonzero $R_{56,\mathrm{LH}}$, one can remove bunching at certain frequencies due to the energy modulation accumulated from the gun to the laser heater [58]. Mathematically the two terms in the square bracket of Eq. (5) compensate each other. Overall, these results indicate a significant impact of MBI, sensitive to the lattice R_{56}, on the energy spread.

Figures 4 and 5 display the measured energy spread as a function of the electron beam peak current and average β function along the lattice, respectively. In both cases, the values are shown for nominal and zero R_{56} in both chicanes. The peak current scan was done for the optics with the lowest β function, close to standard settings. The optics scan was performed for the standard peak current of about 20 A. We measured the energy spread for an average β function of 15, 23, and 63 m for nominal R_{56} and 16 and 74 m for $R_{56} = 0$ mm.

One can observe a significant dependence of the energy spread on the R_{56}, the peak current, and the optics. In both scans (current and optics), the energy spread values are much higher when the dispersive sections are set to their nominal values. This again points to significant MBI effects.

Looking at Fig. 4, we see that the energy spread significantly increases with the peak current: from 2.8 ± 0.1 (for 1 A) to 14.2 ± 0.3 keV (for 19 A) for nominal R_{56}, and from 1.4 ± 0.3 keV (for 0.3 A) to 5.9 ± 0.1 keV (for 19 A) for zero R_{56}. This indicates, first of all, that the energy spread is mostly the result of collective effects. Fitting the current dependence measurements with a power function of the type $a + bI^c$, the measurements for nominal R_{56} yield a coefficient $c = 1.07 \pm 0.09$, while the data for zero R_{56} result in $c = 0.33 \pm 0.11$. These numbers are largely consistent with Eqs. (3) and (4): with nominal R_{56},

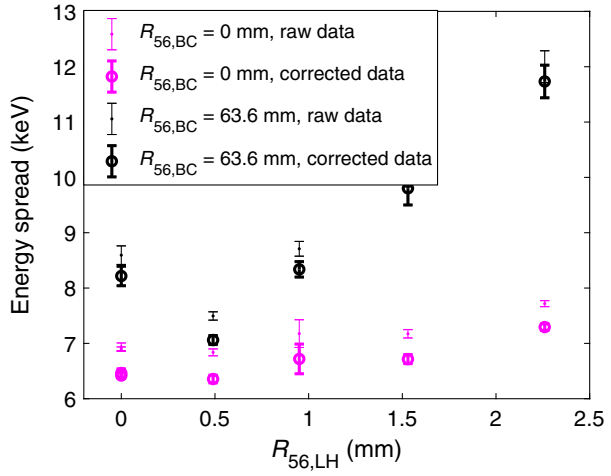

FIG. 3. Measured energy spread as a function of the laser heater and bunch compressor longitudinal dispersion ($R_{56,\mathrm{LH}}$ and $R_{56,\mathrm{BC}}$).

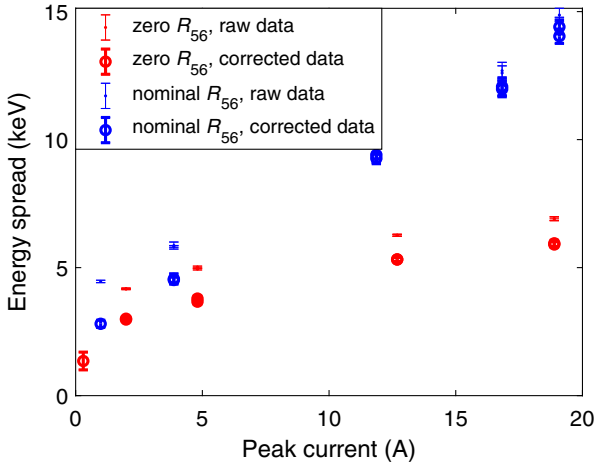

FIG. 4. Energy spread measurements as a function of the peak current of the electron beam for two different R_{56} configurations.

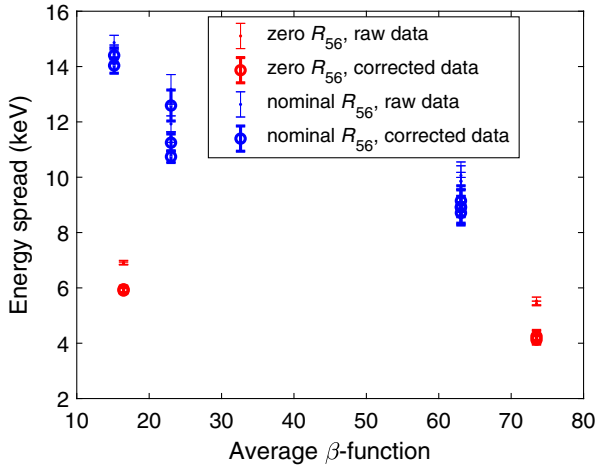

FIG. 5. Energy spread measurements as a function of the lattice optics for two different R_{56} configurations.

we have both MBI and IBS and the power function coefficient is around unity, while with $R_{56} = 0$ mm, there is no significant MBI and mostly IBS plays a role, resulting in a power coefficient closer to the expected 0.5. These results stress that IBS dominates the energy spread behavior for zero R_{56}, while MBI does so for nonzero R_{56} (as long as the MBI is large enough).

Figure 5 shows that the energy spread also depends on the β function of the lattice: it decreases from 14.2 ± 0.3 to 8.9 ± 0.5 keV when the average β function increases from 15 to 63 m for nominal R_{56} configuration, and from 5.9 ± 0.1 to 4.2 ± 0.2 keV when the average β function goes from 16 to 74 m for zero R_{56}. This behavior suggests an impact of IBS, the effects of which depend on the lattice optics. As expected from Eq. (3), the energy spread decreases with larger β functions. For this case, there is no enough data for a proper fit of a power function. However, we can scale the values at high β function from the measurement at the lowest β according to Eq. (3): 14.2 keV for a β function of 15 m (nominal R_{56}) would correspond to 12.8 keV for a β function of 23 m, and to 9.9 keV for a β function of 63 m; and 5.9 keV for a β function of 16 m ($R_{56} = 0$ mm) are expected to decrease to 4.0 keV for a β of 74 m. This fits quite well with the measured data: 11.5 ± 0.4 keV for $\beta = 23$ m and 8.9 ± 0.5 keV for $\beta = 63$ m (nominal R_{56}), and 4.2 ± 0.2 keV for $\beta = 74$ m ($R_{56} = 0$ mm).

All in all, the experimental results suggest that both IBS and MBI play a significant role in the energy spread blowup observed at SwissFEL.

C. Comparison to previous results

In Ref. [44], we performed measurements at nominal R_{56} chicane settings for two different bunch charges: the standard bunch charge of 200 pC and a reduced bunch charge of 10 pC. For each condition, we performed an energy scan to consider resolution effects. The measurements were done for a fixed TD voltage. We did not measure the peak current at that time. However, based on previous experience, we expect a peak current of around 20 A for 200 pC and about 3 A for 10 pC. After removing the expected TD contribution, we reconstructed an energy spread of 14.8 ± 0.3 keV for the standard bunch charge and 6.3 ± 0.5 keV for 10 pC. The reconstructed screen resolutions were 33 ± 8 μm and 29 ± 6 μm for the two different conditions. The natural beam size contribution was much smaller than the contributions related to screen resolution and energy spread.

These results are consistent with what we obtained here. First, we reconstruct energy spreads between 11.7 ± 0.3 keV (R_{56} scans on day 2) and 14.2 ± 0.3 keV (day 1 for 20 A or 200 pC and nominal R_{56} settings), which fits within 15% of the 14.8 keV reported in [44]. We do not have a direct measurement for nominal R_{56} and a peak current of 3 A. By extrapolation of the measured values, we would get an energy spread of around 4 keV. This is significantly lower than the 6 keV reported in [44]. The reason could be the lower emittance we had at that time (we reduced the laser iris aperture and measured a normalized emittance of around 90 μm), which results in a higher IBS contribution to the energy spread.

Second, we obtain a screen resolution of 37.5 ± 0.5 μm, within the error bars of what we reconstructed in [44]. Here we performed measurements for higher electron beam energies (604 MeV compared to 430 MeV), which allowed us to determine the monitor resolution with much higher precision. Finally, the natural beam size contributions in the measurements shown here are also much smaller than the other two components.

We have demonstrated that reducing the R_{56} of the dispersive sections helps to improve the energy spread for the nominal charge and optics case. We get a reduction from about 12 to 6 keV when moving from nominal to zero R_{56}. Increasing the β function at the injector helps to further reduce the energy spread. Considering the impact of both the chicanes R_{56} and the optics, we show a reduction of the energy spread from about 12–14 keV to about 4 keV, i.e., an improvement of more than a factor of 3. The 4 keV are still much larger than what is expected from numerical simulations. Based on our observations and the current modeling, we think that the remaining 4 keV are dominated by IBS. Other contributions may be space charge effects in the low-energy part (that amount to less than 1 keV according to ASTRA simulations), cathode effects, quantum fluctuations due to the emission of synchrotron radiation in bending magnets [59], and the SASE interaction in the laser heater modulator. We estimate that the energy spread induced by the latter two effects is well below 1 keV.

V. MODELING

A full and highly detailed simulation with each electron resolved is extremely challenging and beyond the scope of

this work. Instead, we use a simple model aiming to reproduce the measurement results. To describe the growth due to IBS, we use Eq. (2) with a stepwise integration for the variance of the energy

$$\sigma_{\gamma,j+1}^2 = \sigma_{\gamma,j}^2 + \alpha \frac{2r_e^2 N_e}{\epsilon_n \sigma_j \sigma_s} \Delta z_j, \tag{15}$$

where the index j indicates the jth integration step with a step width of Δz_j and α is a possible correction factor to the overall IBS strength. The effective beam size $\sigma_j = \sqrt{\sigma_{x,j}\sigma_{y,j}}$ is derived in advance from particle tracking. For the beam size calculations, we consider a normalized emittance of 150 nm.

The model used is not directly applicable since it is based on the dynamics in a storage ring, where Coulomb scattering events occur over many turns at any position in the ring. This is different for an injector since most of the time the electron motion is predominantly laminar with crossings of the electrons' trajectories only at certain locations, namely the waists in the beam transport. With sufficient betatronic phase advance along the injector, however, the model should become more and more valid. Additionally, Eq. (15) is an approximation in the sense that it limits the maximum relative energy transfer of an electron-to-electron scattering event to 10^{-5}. We take this into account by fitting the numerical model to our experimental results when all dispersion sections were turned off. The resulting correction coefficient is $\alpha = 2.4$ and will be used for all further calculations. This value indicates that assuming a maximum relative energy transfer of 10^{-5} may be too stringent for our case.

For the MBI model, we evaluate the impedance of the longitudinal space charge for various wave numbers and propagate the bunching $b(k)$ and energy modulation $\delta\gamma(k)$ stepwise according to Eqs. (5) and (6). The effective R_{56} per step is calculated as

$$R_{56,j} = \frac{\Delta z_j}{\gamma_j^2} + \hat{R}_{56}(z_j). \tag{16}$$

It combines the run-time difference of a drift and the explicit $\hat{R}_{56}$ for the laser heater, the bunch compressor and injector spectrometer. As with the IBS model, the energy γ_j, beam size σ_j, and $R_{56,j}$ are precalculated, while the uncorrelated energy spread, due to IBS, $\sigma_{\gamma,j}$ is taken from the evaluation of Eq. (15).

Since there is no coupling between the different wave numbers, we can initialize each bunching component with its mean value of $b_0 = 1/\sqrt{N_e}$, a bunching phase of zero degrees and an energy modulation $\delta\gamma_0(k) = 0$ eV. We consider wave numbers in the range between $k_{\min} = 2\pi/(100\ \mu\text{m})$ and $k_{\max} = 2\pi/(1\ \mu\text{m})$. Since these wave numbers are considered too large for being resolved by the measurement, they effectively contribute to the observed energy spread $\tilde{\sigma}_\gamma$ with

$$\tilde{\sigma}_\gamma = \sqrt{\sigma_\gamma^2 + \frac{1}{2}\sum_{i=M_k}^{N_k} \delta\gamma^2(k_i)}. \tag{17}$$

Since the electron bunch has a finite length, we are not allowed to take an arbitrary number of frequency components N_k, because only a limited number of modes in frequency space can be regarded as independent. This is estimated with $N_k \approx k_{\max}/k_b$ and $k_b = 2\pi/L_b$, the bunch wave number for a given bunch length L_b. The starting index is $M_k \approx k_{\min}/k_b$. We verified that enlarging the range of wave numbers has no significant impact on our results.

We had to fine-tune the model by disabling the Landau damping term in the low-energy part of the SwissFEL injector for the first 7 m, since it lowers the mean bunching factor below the shot-noise level. In reality, the rearrangement in the electron position would form a new bunching with a different phase. This cannot be described correctly with the bunching coefficient represented as a collective parameter in the model.

Figure 6 shows the simulation results using this model for the R_{56} and peak current scans, together with the measurement values (with resolution and TD contribution subtracted). As is evident from the figure, the agreement between the model and the experimental data is rather good. In particular, the model reproduces the energy spread reduction when increasing $R_{56,\text{LH}}$ from zero to slightly above. Although the dependences on the different parameters are generally well reproduced, the model underestimates the energy spread at low beam currents, for moderate $R_{56,\text{LH}}$ with nominal $R_{56,\text{BC}}$, and for large $R_{56,\text{LH}}$ with $R_{56,\text{BC}} = 0$ mm.

Our model does not consider the additional Landau damping in the MBI due to betatron oscillations [37], neither the impact of IBS on the transverse emittances [29,30]. We estimate, however, that these effects are negligible in our case. More importantly, the present modeling based on a collective description of the energy modulation and the bunching factor is not suitable to describe effects such as plasma oscillations and its impact to the bunching factor in the first meters of the injector. A better approach would be based on a particle tracking code with no model assumptions, considering the electrons' motion in their own space-charge fields. To our knowledge, GPT is currently the only code capable of performing such a consistent tracking. However, the required time to simulate a typical electron beam (e.g., 200 pC) is too high. We hope that our work stimulates further code and modeling development.

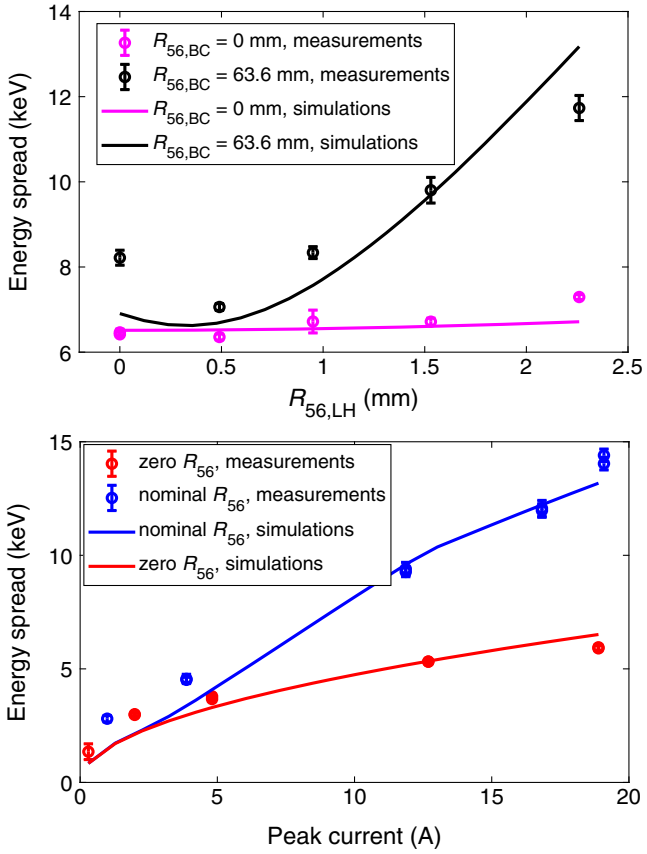

FIG. 6. Measured and simulated dependences on the lattice R_{56} (top) and the peak current of the electron beam (bottom).

VI. CONCLUSION

In [44], we presented a new method to measure the energy spread with high resolution. We reconstructed energy spread values at the SwissFEL injector much higher than predicted by simulations (15 keV for the standard bunch charge of 200 pC). With the aim to understand this deterioration, we have performed energy spread measurements at the SwissFEL injector as a function of electron bunch peak current, lattice optics, and longitudinal dispersion.

We have experimentally demonstrated the capacity of our measurement approach to reconstruct energy spread values of about 1 keV overcoming the resolution limit of the standard approach by a factor of 2. Besides this methodological advance, the measured dependences have shown that the energy spread blowup is caused by both IBS and MBI. The observed dependences can be described by existing IBS and MBI models. For the IBS model, however, a scaling factor of 2.4 is required to fit the results.

For the standard 200-pC case, we have shown that the energy spread can be improved from up to 14 keV to about 6 keV by reducing the R_{56} of the two chicanes and further down to about 4 keV by additionally increasing the lattice β function. These 4 keV may be related to remaining IBS, space-charge, or cathode effects. In the future, we may study the possible impact of the cathode material on the energy spread.

Reducing $R_{56,LH}$ from its nominal value of 2.2 to 1.0 mm (the minimum value at which the laser heater can still be operational) improves the SwissFEL performance: thanks to the reduced energy spread the beam can be more compressed and we obtain higher FEL pulse energies. In the future, we plan to move the bunch compressor of the SwissFEL injector upstream from its current location. By reducing the distance from the gun to the bunch compressor, we will reduce the energy spread deterioration before compression due to effects depending on the distance such as IBS and MBI. After compression, the energy spread is naturally increased, therefore IBS and MBI will have much less impact from there on. The design of the SwisFEL injector in principle allows a reduction of the required length by about 30 m, which would provide IBS with only half the distance to accumulate. An additional advantage is that such a change would free up space that may be filled with more rf stations in the main linac. Another measure to reduce the energy spread would be to change the design optics toward larger β functions.

The measurements shown here represent the first evidence of IBS and MBI in an FEL injector. Our results show the advantage of operating with lower R_{56}, with large β functions in the lattice, and with a small distance between the electron source and the first bunch compressor. These findings may be of importance for the design of present and future FEL facilities based on ultrabright electron beam sources (see, e.g., Refs. [15,16,60]). Furthermore, our evaluations indicate that standard tools to model electron beam sources, not covering the observed physics effects, are insufficient and that new approaches are required.

ACKNOWLEDGMENTS

We acknowledge all the technical groups involved in the operation of SwissFEL. The work of P. D. in the context of this project was supported by the Swiss National Science Foundation under Grant No. 200021_175498.

[1] J. B. Hastings, F. M. Rudakov, D. H. Dowell, J. F. Schmerge, J. D. Cardoza, J. M. Castro, S. M. Gierman, H. Loos, and P. M. Weber, Ultrafast time-resolved electron diffraction with megavolt electron beams, Appl. Phys. Lett. **89**, 184109 (2006).

[2] P. Musumeci, J. Moody, and C. Scoby, Relativistic electron diffraction at the UCLA Pegasus photoinjector laboratory, Ultramicroscopy **108**, 1450 (2008).

[3] S. Boucher, P. Frigola, A. Murokh, M. Ruelas, I. Jovanovic, J. Rosenzweig, and G. Travish, Inverse compton scattering gamma ray source, Nucl. Instrum. Methods Phys. Res., Sect. A **608**, S54 (2009).

[4] W. Graves, W. Brown, F. Kaertner, and D. Moncton, MIT inverse compton source concept, Nucl. Instrum. Methods Phys. Res., Sect. A **608**, S103 (2009).

[5] Z. Huang and K.-J. Kim, Review of x-ray free-electron laser theory, Phys. Rev. ST Accel. Beams **10**, 034801 (2007).

[6] B. W. J. McNeil and N. R. Thompson, X-ray free-electron lasers, Nat. Photonics **4**, 814 (2010).

[7] C. Pellegrini, A. Marinelli, and S. Reiche, The physics of x-ray free-electron lasers, Rev. Mod. Phys. **88**, 015006 (2016).

[8] J. S. Fraser, R. L. Sheffield, E. R. Gray, and G. W. Rodenz, High-brightness photoemitter injector for electron accelerators, IEEE Trans. Nucl. Sci. **32**, 1791 (1985).

[9] C. Hernandez-Garcia, P. G. O'Shea, and M. L. Stutzman, Electron sources for accelerators, Phys. Today **61**, No. 2, 44 (2008).

[10] M. Schaer, A. Citterio, P. Craievich, S. Reiche, L. Stingelin, and R. Zennaro, rf traveling-wave electron gun for photoinjectors, Phys. Rev. Accel. Beams **19**, 072001 (2016).

[11] B. E. Carlsten, P. M. Anisimov, C. W. Barnes, Q. R. Marksteiner, R. R. Robles, and N. Yampolsky, High-brightness beam technology development for a future dynamic mesoscale materials science capability, Instruments **3**, 52 (2019).

[12] R. R. Robles, O. Camacho, A. Fukasawa, N. Majernik, and J. B. Rosenzweig, Versatile, high brightness, cryogenic photoinjector electron source, Phys. Rev. Accel. Beams **24**, 063401 (2021).

[13] A. R. Maier, A. Meseck, S. Reiche, C. B. Schroeder, T. Seggebrock, and F. Grüner, Demonstration Scheme for a Laser-Plasma-Driven Free-Electron Laser, Phys. Rev. X **2**, 031019 (2012).

[14] T. André, I. A. Andriyash, A. Loulergue, M. Labat, E. Roussel, A. Ghaith, M. Khojoyan, C. Thaury, M. Valléau, F. Briquez *et al.*, Control of laser plasma accelerated electrons for light sources, Nat. Commun. **9**, 1334 (2018).

[15] A. Deng, O. S. Karger, T. Heinemann, A. Knetsch, P. Scherkl, G. G. Manahan, A. Beaton, D. Ullmann, G. Wittig, A. F. Habib *et al.*, Generation and acceleration of electron bunches from a plasma photocathode, Nat. Phys. **15**, 1156 (2019).

[16] J. B. Rosenzweig, N. Majernik, R. R. Robles, G. Andonian, O. Camacho, A. Fukasawa, A. Kogar, G. Lawler, J. Miao, P. Musumeci *et al.*, An ultra-compact x-ray free-electron laser, New J. Phys. **22**, 093067 (2020).

[17] R. Bonifacio, C. Pellegrini, and L. M. Narducci, Collective instabilities and high-gain regime in a free electron laser, Opt. Commun. **50**, 373 (1984).

[18] A. Malyzhenkov, Y. P. Arbelo, P. Craievich, P. Dijkstal, E. Ferrari, S. Reiche, T. Schietinger, P. Juranić, and E. Prat, Single- and two-color attosecond hard x-ray free-electron laser pulses with nonlinear compression, Phys. Rev. Res. **2**, 042018(R) (2020).

[19] L. H. Yu, Generation of intense UV radiation by subharmonically seeded single-pass free-electron lasers, Phys. Rev. A **44**, 5178 (1991).

[20] E. Allaria, D. Castronovo, P. Cinquegrana, P. Craievich, M. D. Forno, M. B. Danailov, G. D'Auria, A. Demidovich, G. D. Ninno, S. D. Mitri *et al.*, Two-stage seeded soft-x-ray free-electron laser, Nat. Photonics **7**, 913 (2013).

[21] P. R. Ribič, A. Abrami, L. Badano, M. Bossi, H.-H. Braun, N. Bruchon, F. Capotondi, D. Castronovo, M. Cautero, P. Cinquegrana *et al.*, Coherent soft x-ray pulses from an echo-enabled harmonic generation free-electron laser, Nat. Photonics **13**, 555 (2019).

[22] A. Piwinski, Intra-beam-scattering, in *Proceedings of the 9th International Conference on High-energy Accelerators, SLAC, Stanford, CA, USA, 1974* (1974), pp. 405–409, 10.5170/CERN-1992-001.226.

[23] J. D. Bjorken and S. K. Mtingwa, Intrabeam scattering, Part. Accel. **13**, 115 (1983).

[24] K. Kubo and K. Oide, Intrabeam scattering in electron storage rings, Phys. Rev. ST Accel. Beams **4**, 124401 (2001).

[25] Z. Huang, Intrabeam scattering in an x-ray FEL driver, SLAC, Technical Report No. SLAC-TN-05-026, 2002.

[26] K. L. F. Bane, An accurate, simplified model of intrabeam scattering, SLAC, Technical Report No. SLAC-AP-141, 2002.

[27] K. Kubo, S. K. Mtingwa, and A. Wolski, Intrabeam scattering formulas for high energy beams, Phys. Rev. ST Accel. Beams **8**, 081001 (2005).

[28] S. Di Mitri, G. Perosa, A. Brynes, I. Setija, S. Spampinati, P. H. Williams, A. Wolski, E. Allaria, S. Brussaard, L. Giannessi *et al.*, Experimental evidence of intrabeam scattering in a free-electron laser driver, New J. Phys. **22**, 083053 (2020).

[29] C.-Y. Tsai, W. Qin, K. Fan, X. Wang, J. Wu, and G. Zhou, Theoretical formulation of phase space microbunching instability in the presence of intrabeam scattering for single-pass or recirculation accelerators, Phys. Rev. Accel. Beams **23**, 124401 (2020).

[30] C.-Y. Tsai and W. Qin, Semi-analytical analysis of high-brightness microbunched beam dynamics with collective and intrabeam scattering effects, Phys. Plasmas **28**, 013112 (2021).

[31] G. Perosa and S. D. Mitri, Matrix model for collective phenomena in electron beam's longitudinal phase space, Sci. Rep. **11**, 7895 (2021).

[32] S. Heifets, G. Stupakov, and S. Krinsky, Coherent synchrotron radiation instability in a bunch compressor, Phys. Rev. ST Accel. Beams **5**, 064401 (2002).

[33] Z. Huang and K.-J. Kim, Formulas for coherent synchrotron radiation microbunching in a bunch compressor chicane, Phys. Rev. ST Accel. Beams **5**, 074401 (2002).

[34] E. Saldin, E. Schneidmiller, and M. Yurkov, Klystron instability of a relativistic electron beam in a bunch compressor, Nucl. Instrum. Methods Phys. Res., Sect. A **490**, 1 (2002).

[35] E. Saldin, E. Schneidmiller, and M. Yurkov, Longitudinal space charge-driven microbunching instability in the TESLA Test Facility linac, Nucl. Instrum. Methods Phys. Res., Sect. A **528**, 355 (2004).

[36] Z. Huang, M. Borland, P. Emma, J. Wu, C. Limborg, G. Stupakov, and J. Welch, Suppression of microbunching instability in the linac coherent light source, Phys. Rev. ST Accel. Beams **7**, 074401 (2004).

[37] M. Venturini, Microbunching instability in single-pass systems using a direct two-dimensional Vlasov solver, Phys. Rev. ST Accel. Beams **10**, 104401 (2007).
[38] Z. Huang, A. Brachmann, F.-J. Decker, Y. Ding, D. Dowell, P. Emma, J. Frisch, S. Gilevich, G. Hays, P. Hering *et al.*, Measurements of the linac coherent light source laser heater and its impact on the x-ray free-electron laser performance, Phys. Rev. ST Accel. Beams **13**, 020703 (2010).
[39] S. Spampinati, E. Allaria, L. Badano, S. Bassanese, S. Biedron, D. Castronovo, P. Craievich, M. Danailov, A. Demidovich, G. D. Ninno *et al.*, Laser heater commissioning at an externally seeded free-electron laser, Phys. Rev. ST Accel. Beams **17**, 120705 (2014).
[40] D. Ratner, C. Behrens, Y. Ding, Z. Huang, A. Marinelli, T. Maxwell, and F. Zhou, Time-resolved imaging of the microbunching instability and energy spread at the Linac Coherent Light Source, Phys. Rev. ST Accel. Beams **18**, 030704 (2015).
[41] J. Lee, J.-H. Han, S. Lee, J. Hong, C. H. Kim, C. K. Min, and I. S. Ko, PAL-XFEL laser heater commissioning, Nucl. Instrum. Methods Phys. Res., Sect. A **843**, 39 (2017).
[42] C.-Y. Tsai, Concatenated analyses of phase space microbunching in high brightness electron beam transport, Nucl. Instrum. Methods Phys. Res., Sect. A **940**, 462 (2019).
[43] M. Hüning and H. Schlarb, Measurement of the beam energy spread in the TTF photo-injector, in *Proceedings of the 20th Particle Accelerator Conference, PAC-2003, Portland, OR, 2003* (IEEE, New York, 2003), p. 2074.
[44] E. Prat, P. Dijkstal, E. Ferrari, A. Malyzhenkov, and S. Reiche, High-resolution dispersion-based measurement of the electron beam energy spread, Phys. Rev. Accel. Beams **23**, 090701 (2020).
[45] S. Tomin, I. Zagorodnov, W. Decking, N. Golubeva, and M. Scholz, Accurate measurement of uncorrelated energy spread in electron beam, Phys. Rev. Accel. Beams **24**, 064201 (2021).
[46] H. Qian, M. Krasilnikov, A. Lueangaramwong, X. Li, O. Lishilin, Z. Aboulbanine, G. Adhikari, N. Aftab, P. Boonpornprasert, G. Georgiev, J. Good, M. Gross, C. Koschitzki, R. Niemczyk, A. Oppelt, G. Shu, F. Stephan, G. Vashchenko, and T. Weilbach, Slice energy spread measurement in the low energy photoinjector, Phys. Rev. Accel. Beams **25**, 083401 (2022).
[47] K. Floettmann and V. V. Paramonov, Beam dynamics in transverse deflecting rf structures, Phys. Rev. ST Accel. Beams **17**, 024001 (2014).
[48] K. Flötmann, ASTRA: A space charge tracking algorithm, DESY, Hamburg (2017).
[49] D. Malyutin, Ph.D. thesis, University of Hamburg, 2014.
[50] S. B. van der Geer and M. J. de Loos, General particle tracer: A 3D code for accelerator and beam line design, in *Proceedings of the 5th European Particle Accelerator Conference EPAC 96, Sitges, Barcelona, Spain* (IOP, Bristol, 1996), p. 1245.
[51] J. Qiang, S. Lidia, R. D. Ryne, and C. Limborg-Deprey, Three-dimensional quasistatic model for high brightness beam dynamics simulation, Phys. Rev. ST Accel. Beams **9**, 044204 (2006).
[52] J. Qiang, Y. Ding, P. Emma, Z. Huang, D. Ratner, T. Raubenheimer, M. Venturini, and F. Zhou, Start-to-end simulation of the shot-noise driven microbunching instability experiment at the Linac Coherent Light Source, Phys. Rev. Accel. Beams **20**, 054402 (2017).
[53] V. N. Litvinenko, Y. Jing, D. Kayran, P. Inacker, J. Ma, T. Miller, I. Petrushina, I. Pinayev, K. Shih, G. Wang *et al.*, Plasma-cascade instability, Phys. Rev. Accel. Beams **24**, 014402 (2021).
[54] E. Prat, R. Abela, M. Aiba, A. Alarcon, J. Alex, Y. Arbelo, C. Arrell, V. Arsov, C. Bacellar, C. Beard *et al.*, A compact and cost-effective hard X-ray free-electron laser driven by a high-brightness and low-energy electron beam, Nat. Photonics **14**, 748 (2020).
[55] D. H. Dowell, T. D. Hayward, and A. M. Vetter, Magnetic pulse compression using a third harmonic rf linearizer, in *Proceedings of the Particle Accelerator Conference, Dallas, TX, 1995* (IEEE, New York, 1995), pp. 992–994.
[56] R. Ischebeck, E. Prat, V. Thominet, and C. Ozkan Loch, Transverse profile imager for ultrabright electron beams, Phys. Rev. ST Accel. Beams **18**, 082802 (2015).
[57] E. Prat, P. Dijkstal, M. Aiba, S. Bettoni, P. Craievich, E. Ferrari, R. Ischebeck, F. Löhl, A. Malyzhenkov, G. L. Orlandi *et al.*, Generation and Characterization of Intense Ultralow-Emittance Electron Beams for Compact X-Ray Free-Electron Lasers, Phys. Rev. Lett. **123**, 234801 (2019).
[58] D. Ratner and G. Stupakov, Observation of Shot Noise Suppression at Optical Wavelengths in a Relativistic Electron Beam, Phys. Rev. Lett. **109**, 034801 (2012).
[59] M. Sands, Synchrotron oscillations induced by radiation fluctuations, Phys. Rev. **97**, 470 (1955).
[60] G. D'Auria, M. Aicheler, A. Aksoy, D. Alesini, R. Apsimon, J. M. Arnesano, M. Bellaveglia, A. Bernhard, F. Bosco, B. Buonomo *et al.*, Status of the compact light design study, in *Proceedings of the 39th Free Electron Laser Conference FEL2019, Hamburg, Germany* (JACoW, Geneva, Switzerland, 2019).